

Rapid sintering of high-efficiency phosphor-in-glass films for laser-driven light source

Received: 7 November 2024

Accepted: 7 March 2025

Published online: 21 March 2025



Pengfei Wang^{1,2,3,4}, Hang Lin^{1,2,3}✉, Guoxin Chen⁵, Weitong Weng³,
Yue Xu^{3,4}, Yi Lin³, Ju Xu³, Yao Cheng^{1,3} & Yuansheng Wang^{1,3}✉

The development of advanced high-power-density laser-driven light source requires durable and color-tunable inorganic phosphor-in-glass film composites as color converter. One challenge remains for the phosphor-in-glass film is the thermal erosion and degradation of phosphor, as harsh condition or long duration time is required to densify the film for conventional sintering. Here we develop a rapid thermal annealing technique that achieves high film densification (porosity < 3%) within seconds utilizing high-power (>10 kW) infrared irradiation. As demonstrated by high-resolution electron microscopy observation, a trivial interfacial reaction occurs, leading to almost intact phosphor particles and thus restrained luminous loss. For instance, the red-emitting $\text{Sr}_{0.8}\text{Ca}_{0.2}\text{AlSiN}_3\text{:Eu}^{2+}$ exhibits a record internal quantum efficiency of 91.2% in the processed film and achieves a luminous flux of 2379 lm and efficacy of 140 lm W⁻¹ after fabricating a phosphor wheel. This method reduces energy consumption, enables high-throughput screening, and offers material universality and design flexibility, paving the way for new opto-functional materials and applications.

As the domain of lighting technology strides towards high brightness and environmental consciousness, laser-driven light source has garnered significant attention for its high-power density and wall-plug efficiency¹. In the construction of laser lighting systems, nitride and oxynitride phosphors play a pivotal role as color converters, with importance equally standing with the classical garnet phosphors². The dense crystal structure confers enhanced structural rigidity and thus thermal stability upon these compounds, while the rich and diverse local coordination environment affords greater control over the energy level positions of the doped rare earth luminescence centers. These merits are essential for the overall performance of the laser lighting systems, beneficial to attaining not only high lumen output, but also high color rendering index (CRI), optimal correlated color temperature (CCT) and wide color gamut³.

Laser lighting calls for new phosphor bulk material form with high performance. Traditional phosphor encapsulation, such as those utilizing organic silicone resins as the encapsulation medium to produce phosphor-in-silicone (PiS) composite, has encountered a performance bottleneck. PiS materials are prone to aging at high temperatures, so their thermal stability and durability are often challenged^{4,5}. To address this issue, researchers have begun to explore all-inorganic color converters, such as fluorescent single crystals^{6,7}, fluorescent ceramics^{8–11}, phosphor-in-ceramic (PiC)^{12,13}, phosphor-in-glass (PiG)^{4,14–17}, and phosphor-in-glass films (PiGF)^{18–26}. Unlike garnet oxides, nitrides and oxynitrides are unable to grow into single crystals due to their anisotropy; moreover, their low diffusion coefficients make it challenging to fully densify them into ceramics with acceptable optical properties using traditional methods³. Compounding and encapsulating them with amorphous glass, which is inherently flowable when softened or

¹State Key Laboratory of Structural Chemistry, Fujian Institute of Research on the Structure of Matter, Chinese Academy of Sciences, Fuzhou, Fujian, China.

²Fujian Science & Technology Innovation Laboratory for Optoelectronic Information of China, Fuzhou, Fujian, China. ³Fujian Key Laboratory of Nanomaterials, Fujian Institute of Research on the Structure of Matter, Chinese Academy of Sciences, Fuzhou, Fujian, China. ⁴University of Chinese Academy of Sciences, Beijing, China. ⁵Public Technology Center, Ningbo Institute of Materials Technology and Engineering, Chinese Academy of Sciences, Ningbo, Zhejiang, China.

✉ e-mail: lingh@fjirsm.ac.cn; yswang@fjirsm.ac.cn

melted, would be an advisable choice. The PiG composite displays unparalleled benefits in terms of cost-effectiveness, easy fabrication, and design versatility, when compared to other potential alternatives. Particularly, the sintering of PiG in the form of thick film on a substrate with high thermal conductivity will significantly alleviate luminescence saturation phenomenon under high power densities of lasers. To date, there have been great endeavors paid with the aim of developing high-performance PiG and PiGF. Nevertheless, the conventional preparation process always requires high-temperature and long-duration sintering, which consumes a considerable amount of energy and inevitably brings about phosphor degradation, chemical erosion, and especially oxidation in the case of nitride and oxynitride phosphors^{15,27}. In this regard, the development of a novel sintering technology to fabricate PiG/PiGF in rapid manner is a pressing necessity (Supplementary Note 1), yet it remains a formidable challenge due to the difficulty of material densification. In addition, the up-to-date fast sintering technologies are usually hard to popularize, since the cost and effectiveness are compromised^{8,28–33}. Recently, Xia et al. smartly develop a rapid synthesis technique to fabricate phosphor-glass composites in seconds based on particle self-stabilization, unfortunately just like many other fast sintering strategies, the material system is limited to garnet oxides³⁴.

In this work, we innovatively introduced rapid thermal annealing (RTA), a fast sintering technique previously used in semiconductor manufacturing processes, to prepare PiGF. We demonstrated that RTA technology, which is characterized by extremely high heating rate of up to $55\text{ }^{\circ}\text{C s}^{-1}$, is able to achieve densification of PiGF within seconds, significantly enhancing production efficiency and reducing energy consumption. Taken the red-emitting $\text{Sr}_{0.8}\text{Ca}_{0.2}\text{AlSiN}_3\text{:Eu}^{2+}$ (SCASN:Eu) nitride phosphor as an example, the fabricated SCASN:Eu PiGF via RTA exhibits restrained interfacial reaction between phosphor particles and glass matrix, resulting in an impressive internal quantum efficiency (IQE) of up to 91.2% under 455 nm blue light excitation. This value exceeds those reported for all-inorganic red phosphor bulk materials in the literature. Such a high IQE in red-emissive color converter endows lighting sources based on PiGF with enhanced brightness and comfortable visual experience. RTA technology can be extended to various nitride and oxynitride PiGFs, including, but not limited to, $\text{La}_3\text{Si}_6\text{N}_{11}\text{:Ce}$ (LSN:Ce), $\text{BaSi}_2\text{O}_2\text{N}_2\text{:Eu}^{2+}$ (BaSiON:Eu), $\text{CaAlSiN}_3\text{:Eu}^{2+}$ (CASN:Eu), $\beta\text{-SiAlON:Eu}^{2+}$ ($\beta\text{-SiAlON:Eu}$), and $\alpha\text{-SiAlON:Eu}^{2+}$ ($\alpha\text{-SiAlON:Eu}$), as well as other substrate materials and opto-functional polycrystalline. Such scalability endows the RTA with potential application value across different phosphor systems and various application scenarios, demonstrating the great design flexibility and universality of this technology. More importantly, the uniform temperature field of the RTA technology enables high-throughput screening of materials that can rapidly validate theoretical predictions, hopefully accelerating the discovery of a variety of new PiGF materials.

Results

Fabrication of PiGF via RTA technology

Figure 1a illustrates the PiGF fabrication process via the RTA method. Initially, nitride phosphors, glass powder, and an organic colloid composed of terpineol and ethyl cellulose are homogeneously mixed in a predetermined ratio (Mixing). Subsequently, the uniformly mixed slurry is applied evenly onto a substrate with high thermal conductivity using an automatic coating machine (Coating). Thereafter, the coated precursor film is subjected to a drying process in an oven at $150\text{ }^{\circ}\text{C}$ to remove the organic carrier (Drying). Ultimately, the dried precursor film is sintered within the RTA device to obtain the PiGF. Figure 1b and the Supplementary Fig. 1 provide an overview of how the RTA works and a digital photograph. As depicted in Fig. 1b, the chamber of the RTA unit contains 13 kilowatt-grade tungsten halogen lamps, thermocouple, quartz holder, and other components. The heating lamps are symmetrically distributed across the upper and lower surfaces of

the chamber, radiating energy onto the surface of PiGF sample and monocrystalline silicon wafer positioned on the quartz holder. The silicon wafer, with a bandgap energy of 1.12 eV, strongly absorbs the radiation energy ($\geq 1.12\text{ eV}$) with a black-body radiation spectrum from lamps mainly distributed in the infrared region, and then conducts it to the supported substrate with high thermal conductivity. The PiGF material completes the sintering process in approximately 10 s under the synergistic effect of the halogen lamps' thermal radiation and the silicon wafer's thermal conduction. The metal chamber is cooled by a circulating water system, while the lamps and quartz chamber are cooled by compressed air.

To delineate the distinctions between RTA technology and traditional muffle furnace sintering, the heating rate plots were recorded as shown in Supplementary Fig. 2. In contrast to traditional sintering methods, RTA sintering can rapidly achieve the target temperature from room temperature at a heating rate of $-55\text{ }^{\circ}\text{C s}^{-1}$ (Supplementary Movie 1). Such a short processing duration not only signifies an efficient synthesis methodology but also suggests a reduced energy consumption, amounting to merely 4.3% of that required by conventional sintering techniques (the inset of Supplementary Fig. 2 and Supplementary Note 2). The finite element method (please find the details in the section of "Methods") was used to simulate the heating curve and the temperature distribution on the surface of samples within the RTA equipment as it was heated to $550\text{ }^{\circ}\text{C}$ (Fig. 1c). The simulation results demonstrate the temperature rise proceeds in fast speed (Fig. 1d and Supplementary Movie 2), thanks to the ultra-high temperature of lighting source up to $>3000\text{ K}$. Unlike the real situation, the simulation does not take into account the electrical feedback, which should be responsible for the differences during the heating and soaking stages. A large discrepancy is observed in the cooling stage, majorly attributed to the exclusion of the metal enclosure and the water- and air-cooling systems in the simulation domain. Importantly, the temperature distribution across the silicon wafer is uniform, with a temperature difference of no more than $3\text{ }^{\circ}\text{C}$ between the center and the edge of wafer, and a difference of no more than $1\text{ }^{\circ}\text{C}$ within the area of wafer where samples are placed (Fig. 1e). This confirms that multiple samples experience almost identical sintering conditions in the RTA process, thereby rendering this process suitable for large-scale manufacturing and high-throughput screening.

High-throughput fast screening and universality

RTA technology enables the swift and reliable synthesis of PiGF, facilitating the rapid validation of the compatibility between various glass matrices and a range of phosphors, thereby accelerating the screening process for high-performance PiGF materials (Fig. 2a). As a proof-of-concept experiment, we utilized a model system comprising five common commercial nitride and oxynitride phosphors (SCASN:Eu, CASN:Eu, $\beta\text{-SiAlON:Eu}$, $\text{BaSi}_2\text{O}_2\text{N}_2\text{:Eu}$, and LSN:Ce) and five commercial glass powders (GC825, GF45A, FD233, FD238, and NL-4) to demonstrate the rapid screening capability afforded by the RTA technology. The comprehensive details of the commercial glasses we used, including their composition, glass transition temperature (T_g), softening temperature (T_s), melting temperature (T_m), packed density, average particle size (D50) and refractive index, are summarized in Supplementary Table 1. The related thermophysical parameters are derived from differential thermal analysis (DTA), as presented in Supplementary Fig. 3. As depicted in Fig. 2b, we employed a 5×5 matrix setup to rapidly sinter 25 PiGFs on sapphire substrates at $550\text{ }^{\circ}\text{C}$ for 10 s in one time. The quantum yield test results indicate that different phosphors have distinct optimal glass powders for compatibility under this sintering condition. The external quantum efficiency (EQE) reveals that the most compatible glass matrix for SCASN:Eu and CASN:Eu is NL-4, while for LSN:Ce and $\text{BaSi}_2\text{O}_2\text{N}_2\text{:Eu}$, it is FD238, and for $\beta\text{-SiAlON:Eu}$, it is GF45A. The optimal combination of phosphor and glass will get varied under different sintering temperatures and

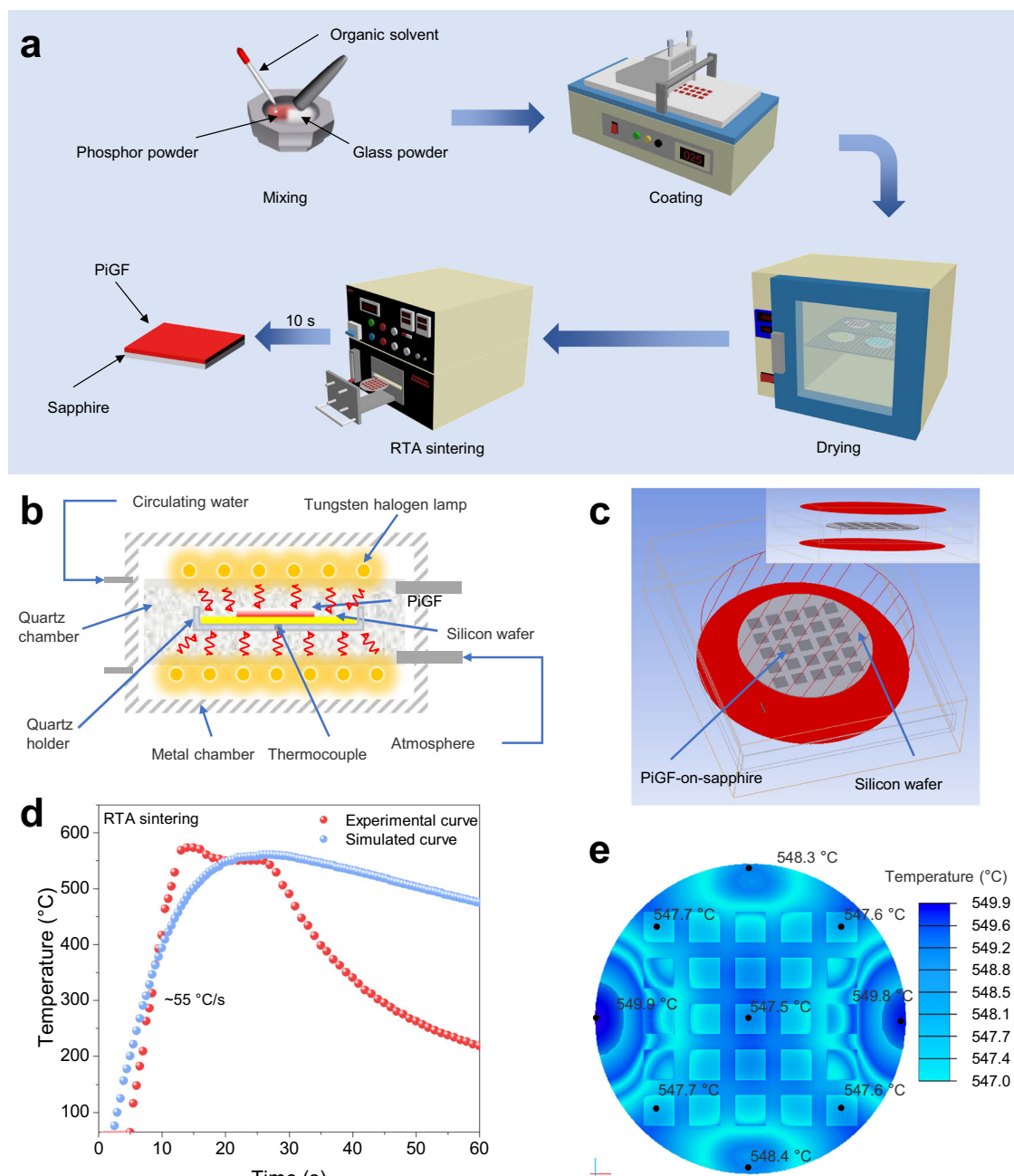


Fig. 1 | Rapid sintering process. **a** Schematic illustration of the synthesis process of phosphor-in-glass film (PiGF) via the rapid thermal sintering (RTA) technology. **b** Internal structure of the RTA device. **c** 3D model for finite element simulation; 5×5 samples are placed on the monocrystalline Si wafer and subjected to irradiation from two planar radiation sources. **d** Experimental and simulated heating

curves for the RTA sintering process; the experimental data are collected in every 0.5 s. **e** Temperature distribution on the wafer surface simulated using finite element analysis at the target temperature of 550 °C. Source data are provided as a Source Data file.

durations (Supplementary Figs. 4, 5). To swiftly ascertain the optimal sintering temperature for various glass matrices, we selected SCASN:Eu as the subject of our study and prepared a series of SCASN:Eu-PiGFs sintered for 10 s at different temperatures in combination with five distinct glass matrices. This experiment was repeated four times and the total time spent was less than 10 min. The EQEs of these samples are summarized in Fig. 2c, showing that the combination of SCASN:Eu with NL-4 exhibits the highest EQE when sintered at 550 °C. One can also find that the optimal sintering temperature varies for different glass matrices.

To achieve the red SCASN:Eu PiGF with the utmost quantum efficiency, a meticulous optimization of the RTA process was

conducted by using the screened NL-4 glass as matrix. The precursor film samples were sintered under different temperatures of 500 °C, 550 °C, 600 °C, 650 °C, and 700 °C, each with a fixed heating duration of 10 s and a varied holding time of 1 s, 5 s, 10 s, 20 s, and 30 s, respectively. In Fig. 2d–f, we show the collection of glass films and SCASN:Eu PiGF combined with sapphire substrate. The corresponding heating curves of RTA process are presented in Supplementary Fig. 6. The transmittance of the glass film, the internal quantum efficiency (IQE) and the EQE of the PiGF were employed as criteria for evaluation. The optimal RTA sintering process at 550 °C for 10 s yields the highest transmittance for the glass film (Fig. 2g), and simultaneously achieving the highest IQE and EQE for the PiGF (Fig. 2h, i). Too lower the

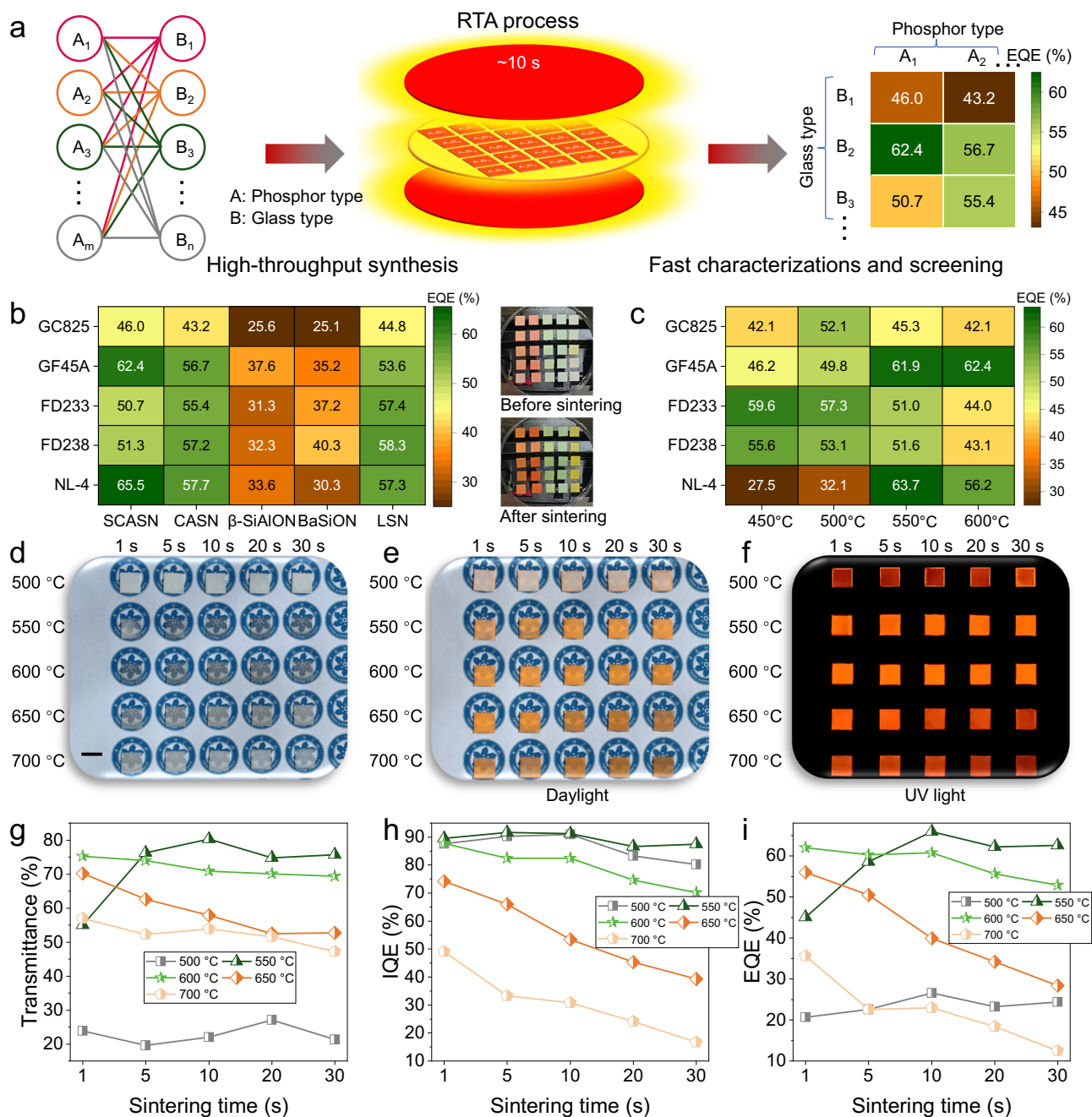


Fig. 2 | High-throughput synthesis and screening. **a** Schematic diagram of the process of high-throughput synthesis and screening of phosphor-in-glass films (PiGFs). A: phosphor type ($i = 1 - m$); B: glass type ($j = 1 - n$). **b** The table shows the external quantum efficiency (EQE) values of PiGFs prepared by rapid thermal annealing (RTA) with different combinations of phosphors and glasses. The insets show digital photographs of a 5×5 matrix of 25 PiGFs before (top) and after (bottom) RTA sintering in daylight. **c** The table shows the EQE values of PiGFs

prepared by RTA at different temperatures with different combinations of SCASN:Eu phosphors and glasses. **d** Digital photograph of the sintered glass films prepared by RTA in daylight. Digital photographs of SCASN:Eu PiGFs prepared by RTA (e) in daylight and (f) under UV light. Scale bar = 1 cm. **g** Transmittance at 800 nm for the glass films prepared by RTA. **h** Internal quantum efficiency (IQE) and (i) EQE values of SCASN:Eu PiGFs. Source data are provided as a Source Data file.

temperature or too shorter the holding time cannot densify the glass film; while in the opposite, the thermal erosion effect takes place that degrades the luminescent performance. To be mentioned, a decrease in the transmittance of the glass film is found when overheating. This phenomenon can be attributed to the volatile constituents within the glass film, which are prone to evaporate during the sintering process and then to leave behind voids (Supplementary Fig. 7). The weight loss of glass supports the hypothesis of substance volatilization (Supplementary Table 2). As a reference, employing the same analytical

approach, we have determined that the most efficacious conditions for traditional sintering to be at 650 °C for 15 min, as shown in Supplementary Fig. 8. It is evident that the traditional sintering necessitates higher furnace temperatures and prolonged sintering times (typically tens of minutes, or even hours^{18,35,36}) to achieve a densification level comparable to the RTA-processed samples. RTA technique in the presence of the intense infrared radiation provided by high-power halogen tungsten lamps facilitates the rapid densification of glass films at lower temperatures.

Furthermore, RTA technology shows great universality and design flexibility in the synthesis of all types of PiGFs with diverse luminescence properties combined with different substrates. The above has shown the nitride and oxynitride PiGFs sintered on sapphire plate with multi-color emissive properties. Instead of sapphire, SCASN-PiGFs can also be sintered on substrates of SiC, K9 glass, and AlN ceramic with high luminescent performance (Supplementary Fig. 9). Moreover, the phosphor system can be extended to oxides, sulphides and even halides (Supplementary Fig. 10). As for the luminescent performance, we took the RTA processed $\text{Y}_3\text{Al}_5\text{O}_{12}:\text{Ce}^{3+}$ (YAG:Ce) PiGF as an example, which yields IQE reaching as high as 95.5% and high brightness much superior to the commercial YAG:Ce³⁺ PiG products (Supplementary Fig. 11). Moreover, the RTA-processed $\text{K}_2\text{SiF}_6:\text{Mn}^{2+}$ PiGF and $\text{Gd}_2\text{O}_2\text{S}:\text{Tb}^{3+}$ PiGF, with the embedded phosphors normally susceptible to thermal degradation, have an acceptable IQE of 72.6% and 58.2%, respectively (Supplementary Figs. 12, 13). Beyond the fluorescent PiGFs, the persistent luminescence PiGFs can be also fabricated via RTA (Supplementary Fig. 14), indicating that RTA-processed materials have broad application scenarios in the other photonic fields such as night vision, anti-counterfeiting, optical storage, etc.

Microstructure of the RTA processed PiGF

We first studied the microstructural evolution of glass precursor during the RTA process. Scanning electron microscopy (SEM) characterization was performed on the glass film samples treated at 550 °C for 1 s, 3 s, 5 s, 7 s, and 10 s, respectively (Fig. 3a). The silicate glass powders used have irregular shape with a D50 particle size of 6 μm after grinding and sieving (Supplementary Fig. 15). At the onset of 1 s RTA process, the glass powder particles are distinctly separated without apparent adhesion (Fig. 3a, i). As the sintering time progresses, the glass frit particles begin to adhere and coalesce with adjacent particles, and simultaneously some large pores are formed by consuming small pores (Fig. 3a, ii–iv). In the final stage of the sintering process, one can see the large pores are expelled out and a uniformly dense glass film devoid of obvious pores or cracks is obtained (Fig. 3a, v). Micro computed tomography (Micro-CT) test images of the glass film sintered for 10 s via RTA are shown in Supplementary Fig. 16. It can be observed that the pore size of glass film follows a Gamma distribution with an average value of 4.58 μm, and the porosity is determined to be only 0.52% based on three-dimensional reconstruction analysis (inset of Supplementary Fig. 16), confirming the rapid densification capability of the RTA process for the glass films. X-ray diffraction (XRD) patterns indicate that the sintered glass film possesses an amorphous structure (Supplementary Fig. 17).

SCASN:Eu phosphor powders exhibit a rod-like shape with a D50 of 11 μm (Supplementary Fig. 18). SEM images of the PiGF surface reveal that the dispersed SCASN:Eu²⁺ phosphor particles have no obvious change in morphology and size (Fig. 3c and Supplementary Fig. 19), suggesting insignificant interfacial reactions. The optical microscope examination, X-ray fluorescence (XRF) testing and confocal laser scanning microscope (CLSM) observation on SCASN:Eu PiGF demonstrate the uniform distribution of phosphor particles throughout the glass matrix (Supplementary Movie 3, Supplementary Figs. 20, 21). To analyze porosity of the PiGF, the micro-CT test is also conducted (Fig. 3b). The results indicate a porosity of 2.9%, which is higher than that of glass film sample, but still remarkably dense. It is inferred that the densification of PiGF undergoes glass softening, formation of sintering necks at contact points, wetting, and gradual expulsion of pores, as schematically illustrated in Supplementary Fig. 22. For PiGF, heterogeneous infiltration and wrapping are more difficult and therefore pore expulsion is not as efficient as the case of glass film. In a typical experiment, the measured thickness of the PiGF is 86 μm (Fig. 3d). XRD patterns of the RTA-processed PiGF samples demonstrate that the crystalline diffraction peaks, consistent with the

standard data (PDF#97-016-3204), originate from the embedded SCASN:Eu (Fig. 3e).

Furthermore, a micro-plane containing SCASN:Eu grain and glass matrix was sectioned using focused ion beam (FIB) for transmission electron microscope (TEM) analysis (Fig. 3f). The high-angle annular dark-field scanning transmission electron microscopy (HAADF-STEM) image in Fig. 3g shows a clear boundary representing the interface between SCASN:Eu particle and glass matrix. The SCASN:Eu particle with higher Z-contrast, scattering more electrons, presents bright region. The corresponding energy-dispersive X-ray spectroscopy (EDS) shows the distinct elemental distribution, i.e., Sr, Al, N concentrate in phosphor particle, O enriches in glass matrix, and Si distributes over both, as expected. In comparison, a blurred interface of approximately 20 nm with apparent elemental interdiffusion can be observed for the sample processed by traditional sintering (Supplementary Figs. 23, 24). High-resolution TEM (HRTEM) observation in Fig. 3h demonstrates that the phase transition layer (associated with thermal erosion) usually observed in the traditional sintering process is almost absent in the RTA-processed PiGF. Fast Fourier Transform (FFT) images taken on three representative regions show the typical amorphous halo and single-crystalline diffraction pattern on glass and crystal grain respectively, and both features at the interface. The observed 2-dimensional interplanar spacings are calculated as 1.84 and 2.54 Å, indexing to (222) and (220) facets of SCASN, respectively. The measured angle between the (222) and (220) facets is 44.1°, getting close to the theoretical one of 43.8°. In the enlarged HRTEM observation at the interface (Fig. 3i), one can still identify a vague interdiffusion region with a thickness of 1–2 nm, where the crystalline lattice becomes blurred and some high-density ionic vacancies are clearly observed. Thereupon, it is reasonable to infer that ionic migration occurs at the interface. These results collectively demonstrate the integrity of the phosphor particles in the PiGFs and the capability of the RTA process to significantly suppress interfacial reactions.

Luminescent performance of the RTA processed PiGF

During the traditional sintering of PiG (S-PiGF-TS), the nitride phosphors are invariably oxidized¹⁵. Fortunately, due to the fast RTA sintering process, which requires only 10 s, the oxidation is successfully mitigated in the SCASN:Eu-PiGF-RTA (S-PiGF-RTA). As illustrated in Fig. 4a, the oxidation-induced shift in the emission center is minimal (a mere 3 nm), in contrast to the reference sample which exhibits a more pronounced shift of up to 7 nm. Benefiting from the suppressed interfacial erosion and the relief of oxidation, the internal quantum efficiency (IQE) of S-PiGF-RTA remains as high as 91.2%, which is only 5.3% lower than that of the original powder and much better than that of the S-PiGF-TS (Fig. 4b and Supplementary Table 3). Compared to other red fluorescent materials (ceramics, PiG, PiGF), the present S-PiGF-RTA composite scores the highest IQE (Fig. 4c and Supplementary Table 4). Photoluminescence (PL) decay curves were also examined, where the decay profile of S-PiGF-RTA almost overlaps with that of phosphor powders, showing a luminescence lifetime decrease of only 7%, whereas the S-PiGF-TS exhibits a 13% reduction (Supplementary Fig. 25). Additionally, we examined the thermal stability performance which is crucial in laser lighting applications. The integrated emission intensity of S-PiGF-RTA at 200 °C still retains 90.4% of that at 25 °C (Supplementary Fig. 26), comparable to the SCASN:Eu powder and also superior to the S-PiGF-TS. Comparison of steady-state and transient-state PL characteristics corroborates the superiority of the RTA process over the traditional methods.

To assess the luminescence properties of the fabricated PiGFs under blue laser excitation, a series of RTA processed S-PiGF phosphor wheels were fabricated with optimization of the phosphor-to-glass

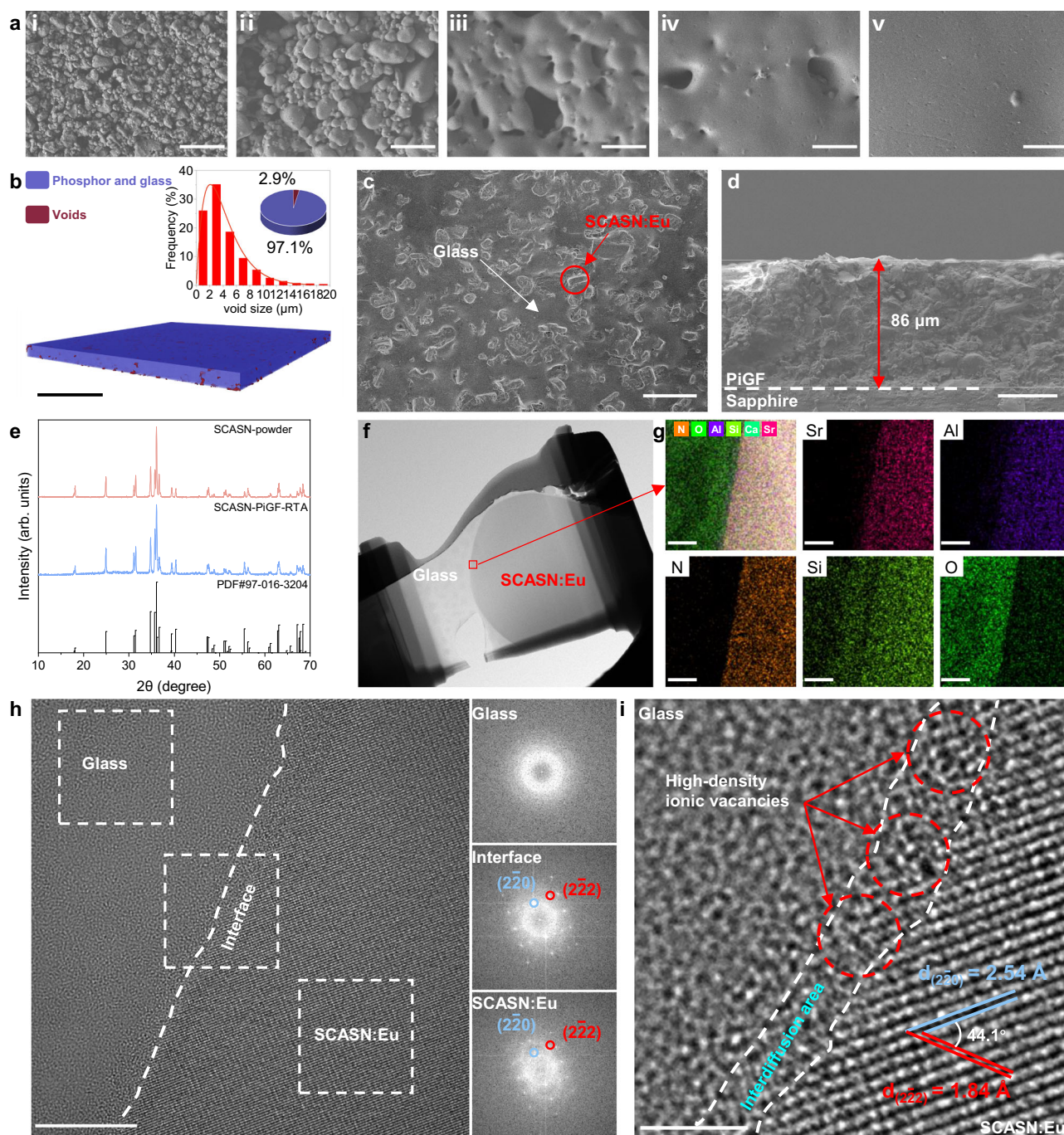


Fig. 3 | Microstructure. **a** SEM images of glass films at different sintering times of (i) 1 s, (ii) 3 s, (iii) 5 s, (iv) 7 s and (v) 10 s, respectively. Scale bar = 5 μ m. **b** Micro-CT 3D images of the phosphor-in-glass film (PiGF) sintered for 10 s; the inset shows void size distribution of glass film and the quantitative analysis of porosity (observation volume: $1000 \times 1000 \times 86 \mu\text{m}^3$; analysis limit: 500 nm). Scale bar = 200 μ m. **c** SEM image on the surface of SCASN:Eu phosphor-in-glass film (PiGF) sintered at 10 s. SCASN:Eu and glass are easily distinguished. Scale bar = 50 μ m. **d** SEM image on the cross section of SCASN:Eu PiGF sintered at 10 s. The interface between PiGF and sapphire is clear. Thicknesses of film: 86 μ m. Scale bar = 50 μ m. **e** XRD patterns of the phosphor powders and the corresponding rapid sintering annealing (RTA)

processed PiGF (SCASN-PiGF-RTA). **f** TEM image of one micro-plane of PiGF sectioned by FIB. Further magnification of the part of the red circle is observed. Scale bar = 2 μ m. **g** Elemental distribution of phosphor particles and glass matrix near the interface. Scale bar = 100 nm. **h** HRTEM image taken near the interface, right panels show FFT images of the corresponding regions. Scale bar = 10 nm. **i** Magnified HRTEM image at the interface. A vague interdiffusion region (white dashed line) with a thickness of 1–2 nm is observed, in which some high-density ionic vacancies (red dashed circle) can be clearly observed. Scale bar = 2 nm. Source data are provided as a Source Data file.

(PtoG) weight ratio and film thickness (Supplementary Fig. 27). The corresponding EL spectra are presented in Supplementary Figs. 28, 29. The adoption of phosphor wheel configuration is based on the consideration of ease of thermal management under dynamic excitation due to more efficient heat convection to air and pulsed irradiation³⁶. It

can be observed that the sample with a PtoG weight ratio of 1:1 and a film thickness of 86 μ m achieves the maximum luminous flux (LF) of 1004 lm under 455 nm blue laser irradiation at a power density of 27 W mm^{-2} . Too heavy the phosphor load or too thick the film leads to the severe heat accumulation and then the thermal runaway effect²¹. A

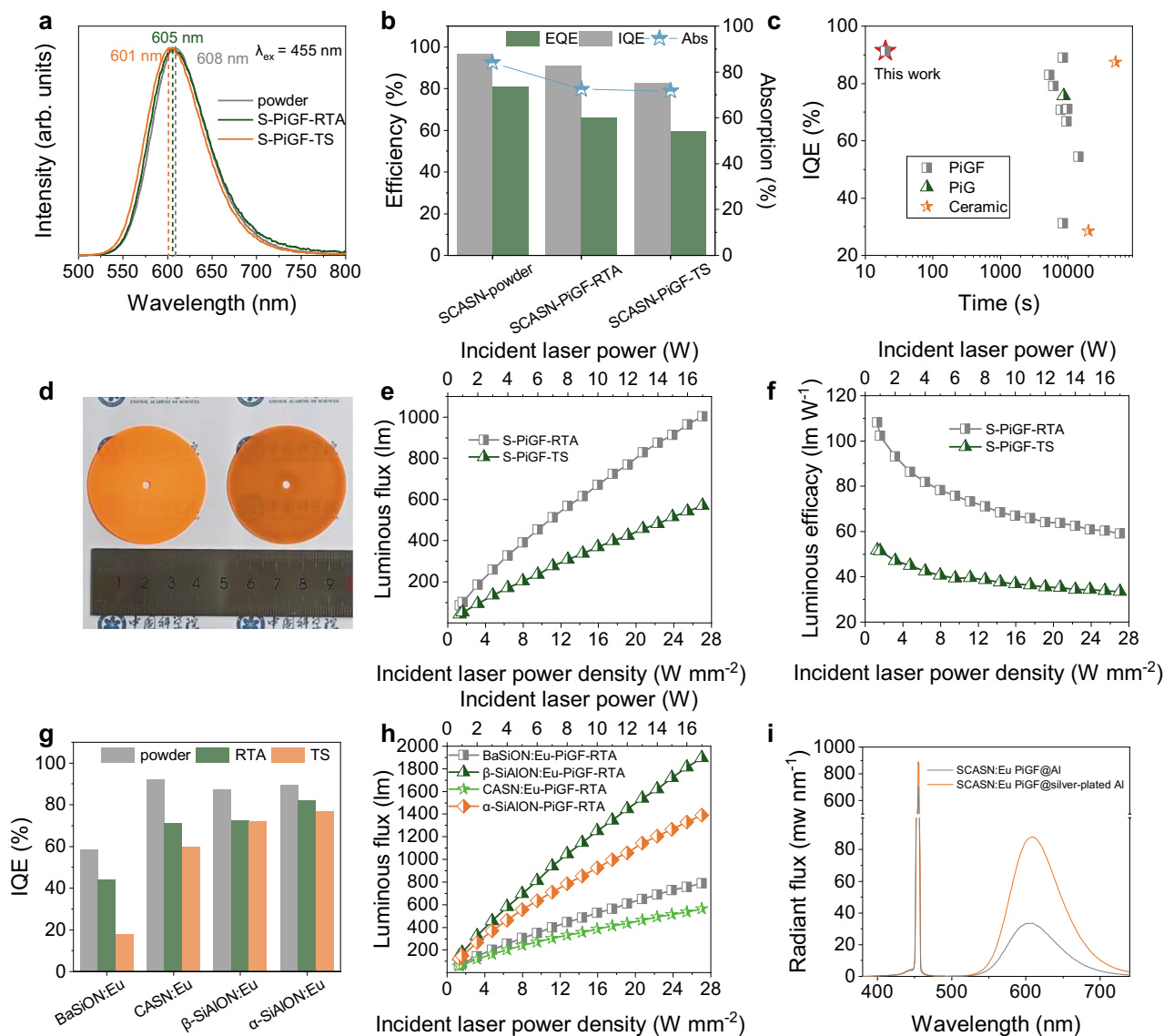


Fig. 4 | Luminescent performances. Comparison on **a** PL spectra, **b** Internal/external quantum efficiency (I/EQE) and absorption efficiency (Abs) of the SCASN:Eu phosphor-in-glass film (PiGF) fabricated by traditional sintering (TS) and rapid thermal annealing (RTA); the data of original phosphor powders are also presented for references. **c** IQE of SCASN:Eu phosphor-in-glass film prepared by RTA (S-PiGF-RTA) as compared with those reported red all-inorganic material (see details in Supplementary Table 4). **d** Digital photograph of the phosphor wheels. **e** Luminous flux and **f** luminous efficacy of the phosphor wheels as a function of the incident laser power and power density. **g** IQEs of the fabricated nitride and oxynitride PiGFs

via the RTA and TS methods and the original phosphor powders. **h** Corresponding Luminous flux values of nitride and oxynitride phosphor wheels prepared by RTA technique as a function of incident laser power and power density. **i** Comparison of EL spectra of SCASN:Eu PiGF phosphor wheels laminated with and without silver-plated aluminum plates under 27 W mm⁻² blue laser excitation. In **e**, **f**, and **h**, the upper x-axis represents the incident laser power, while the lower x-axis represents the incident laser power density; The incident laser power density is calculated by dividing the incident laser power by the spot area (spot area: 0.628 mm²). Source data are provided as a Source Data file.

S-PiGF-TS reference phosphor wheel with the same PtoG weight ratio and thickness is also prepared. There is a large difference in the body color of the samples produced by these two techniques (Fig. 4d), due to the aforementioned difference in the extent of thermal erosion and oxidation. In Fig. 4e, f, the LF and luminous efficacy (LE) are evaluated at different power densities of blue laser. For these two samples, no luminescence saturation occurs up to the power density limit of the present measurement system. At each power density, the S-PiGF-RTA outperforms the S-PiGF-TS, with the LF and LE approximately 1.7 to 2 times higher (Supplementary Table 5), confirming superiority of the RTA-processed PiGF. Of particular note are the thousands of lumens output and 60–100 lm W⁻¹ LE for the blue laser converted red light, which can hardly be achieved with other material forms or preparation techniques.

We employed the same PtoG weight ratio and thickness, and combined them with NL-4 glass to fabricate a series of PiGFs with varying emissive colors, including BaSi₂O₂N₂:Eu, CASN:Eu, β-SiAlON:Eu, and α-SiAlON:Eu, utilizing the RTA technique. Their PL and PLE spectra, along with digital photographs of the samples, are presented in Supplementary Fig. 30. Concurrently, we synthesized comparative samples with the same PtoG weight ratio and thickness using the traditional sintering method. The IQE test results indicate that for the various nitride/oxynitride PiGFs, those prepared using the RTA technique exhibit higher efficiency, as depicted in Fig. 4g and Supplementary Table 6. Brightness tests under blue laser irradiation at different power densities further substantiate this observation (Fig. 4h and Supplementary Figs. 31–35). Furthermore, we have endeavored to enhance the performance of the S-PiGF-RTA phosphor wheel by

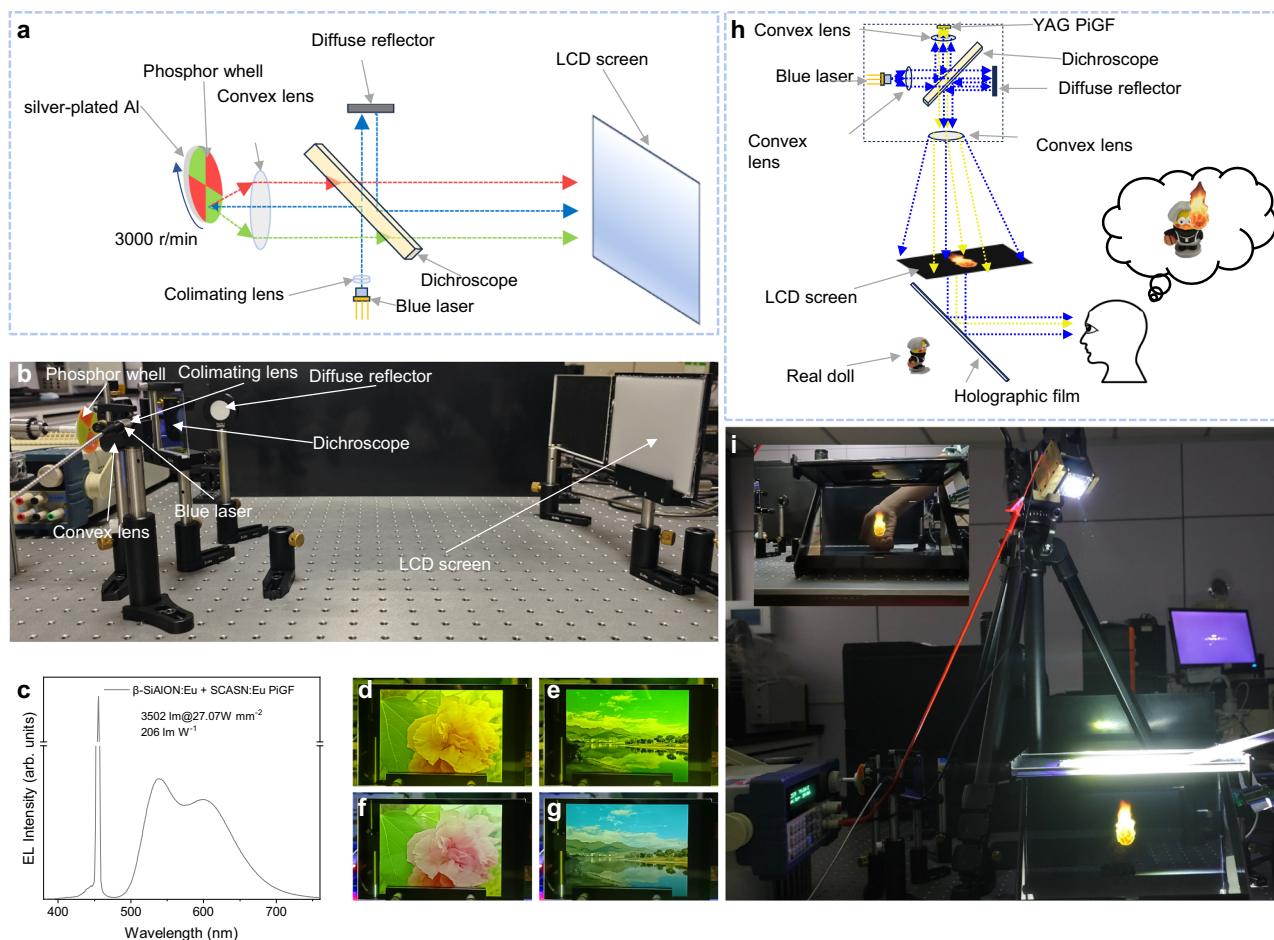


Fig. 5 | Application demonstration. **a** Schematic diagram and **b** digital photograph of the constructed laser-driven display system based on the SCASN:Eu PiGF + β -SiAlON:Eu PiGF phosphor wheel. **c** Corresponding EL spectra of the phosphor wheel converted light source. Laser display visual effect on LCD screen based on **(d, e)** commercial YAG-converted LD light source and **(f, g)** the present PiGF-

converted LD light source. **h** Schematic diagram and **(i)** digital photograph of the constructed holographic display system based on PiGF; inset of **(i)** shows superimposition of virtual flame on a real hand. Source data are provided as a Source Data file.

laminating a silver-coated aluminum sheet on its rear side which helps to collect more back-scattered light³⁷. As shown in Fig. 4i, under the irradiation of a blue laser with a power density of 27 W mm⁻², the output LF of the converted red light has reached a remarkable 2379 lm, with a LE of 140 lm W⁻¹, recording the highest values among the red-emissive color converters we have examined to date (Supplementary Table 7).

Application

To assess the practicality of RTA-processed PiGF for laser-driven light sources, we constructed a display system incorporating a patterned phosphor wheel (Fig. 5a). The physical prototype of the display system is depicted in Fig. 5b. A portion of the blue laser beam sequentially traverses a collimating lens, a dichroic mirror, and a convex lens to irradiate the patterned phosphor wheel integrated with a silver-coated aluminum plate. The other portion of the blue beam is directed towards the primary optical path with the aid of a reflector. Subsequently, the emitted red light from SCASN:Eu, the narrow-band green light from β -SiAlON:Eu, and the blue light along the primary optical path combine to produce white light output. The composed white light is then projected onto an LCD screen, creating the display effect. The spectral distribution, which is a function of the area ratio and thickness of the red-emitting SCASN:Eu PiGF and the green-emitting β -SiAlON:Eu PiGF, has been fine-tuned for optimal display performance. As demonstrated in Fig. 5c, with laser excitation at 27 W mm⁻², the

patterned phosphor wheel achieves a maximum luminous flux of 3502 lm, with a luminous efficacy of 206 lm W⁻¹. Comparative analysis with commercial YAG:Ce-based laser light sources reveals that the laser-driven phosphor wheels, utilizing SCASN:Eu PiGF and β -SiAlON:Eu PiGF as backlight sources, yield more vibrant and visually pleasing effects on the LCD screen, as evidenced in Fig. 5d–g and the Supplementary Movie 4. Furthermore, we delved into the application of laser display technology in holographic projection. By employing a blue laser light source, YAG:Ce³⁺ PiGF prepared via the RTA technology, an LCD screen, and a holographic film, we assembled a rudimentary holographic display cabinet (Fig. 5h). The related working mechanism is presented in Supplementary Note 3. As depicted in Fig. 5i and Supplementary Movie 5, it is evident within the holographic display cabinet that, the virtual three-dimensional (3D) flame is superimposed on the real figurine or hand, achieving an interaction between the virtual and real elements. This showcases the potential of RTA technology in the domain of virtual reality applications.

Discussions

Throughout the research history of PiG/PiGF, a key challenge is how to mitigate interfacial reactions between phosphor particles and glass components during co-sintering to preserve the exceptional luminescent properties of the phosphors. Strategies such as phosphor encapsulation, selecting glass systems with low aggressivity, and employing rapid sintering techniques have been explored^{4,5,16,30,31,33,34,38,39}. Rapid

sintering, in particular, shows promise in reducing the time for ionic migration at interfaces. The present RTA approach utilizes high-power tungsten halogen lamps to quickly elevate the temperature to the desired sintering point within seconds, effectively addressing this challenge. In addition, the RTA approach requires a lower sintering temperature compared to traditional methods due to its unique heating process. The lowered temperature prevents sufficient thermal energy from overcoming the energy barrier for ionic migration, preserving the integrity of the embedded phosphor and maintaining high QE.

From a thermodynamic perspective, an increase in sintering temperature results in a decrease in the viscosity of glass system, leading to enhanced ionic migration between phosphor and glass. While using glass powders with a lower T_s as raw material may seem preferable, the relationship between T_s and QE is not always straightforward, as demonstrated by the RTA screening results (Fig. 2c). Moreover, for the PiGF using glass powders with high T_s , the QE result is not as unfavorable as initially expected (Supplementary Figs. 36, 37). In fact, the high- T_s PiGF sintered at 750 °C for 10 s even shows a higher IQE/EQE (i.e., 63.9%/39.1%) than that (i.e., 16.7%/12.5%) of the low- T_s NL-4 glass sintered at 700 °C for 10 s. Apart from the viscosity of the glass system, the influence of thermally-aggressive glass components should not be underestimated. For high- T_s glass, the presence of thermally-aggressive alkali metal ions is typically lower, thereby impeding ionic migration. It is noteworthy that the absence of alkali metal ions significantly suppresses the interfacial reactions observed in the silica-glass-based YAG:Ce PiG sintered at temperatures up to 1250 °C¹⁷.

For PiGF, the densification occurs through the viscous flow of glass to fill voids among particles or cavities resulting from the evaporation of organic paste during preheating. When utilizing RTA sintering, controlling the film thickness is crucial. In Supplementary Fig. 38, the film processed at 550 °C for 10 s shows large pores and detachment from the sapphire substrate when the film is too thick. This is attributed to the reduced thermal conduction efficiency from the film surface or the supported silicon wafer to the inner part. As a result, the glass flow becomes overly viscous to effectively expel the pores. We have determined that the maximum film thickness compatible with the RTA approach, sintered within seconds, should be kept below ~130 µm. In addition, surface roughness significantly influences the luminescence performance of the PiG product. To assess this, we utilized a 3D white light interferometer to analyze the 3D surface topography of the PiGF (Supplementary Fig. 39). The calculated average surface roughness is 1.096 µm. Considering the satisfactory luminous performance of the manufactured PiGF phosphor wheel, the surface roughness achieved through RTA processing is suitable for practical applications. While a smoother surface could potentially enhance luminous performance, it would entail a notable increase in costs.

In summary, we report a rapid and facile RTA approach to fabricate PiGF composite for the advanced laser-driven light source. High-power infrared light strikes the PiGF and Si substrate, producing massive heat within seconds. Finite element analysis demonstrates the extremely high heating rate and homogeneous heat distribution in the quartz cavity. These properties enable high-throughput screening of PiGF, either to determine phosphor-glass compatibility or to optimize sintering parameters. Microstructural and spectroscopic studies reveal that the RTA technology achieves rapid densification of the PiGF (with porosity < 3%) at lower temperatures compared to traditional sintering methods, beneficial to mitigating the effects of erosion and oxidation, thus preserving the luminescent efficiency of phosphors. We first observe high-density ionic vacancies at the phosphor-glass interface (1–2 nm interdiffusion region) with vague crystal lattice due to ionic migration. RTA technology is especially suitable for those phosphors that are unstable when co-sintered with glass, such as the

rare earth doped (oxy)nitrides of great importance for solid-state lighting, but is also suitable for common garnet oxides and other opto-functional polycrystalline phosphor and persistent phosphor systems. As an example, the RTA-processed SCASN:Eu PiGF scores the highest IQE of 91.2% among the red-emissive inorganic bulk color converters ever reported. Upon driven by 27 W mm⁻² blue laser, the output luminous flux of the converted red light for the corresponding phosphor wheel reaches a remarkable 2379 lm with a LE of 140 lm W⁻¹. Finally, we present demo experiments of the laser-driven light sources designed to create more vivid and visually appealing effects in LCD displays, and to construct a fascinating holographic display with an interaction between the virtual and real elements. The development of RTA technology brings new opportunities to explore more efficient PiGF systems, heralding a bright future for next-generation high-power laser lighting and displays, as well as other emerging photonic applications.

Methods

Raw materials

The glass powders including GC825 (Okamoto Glass Co., Ltd), GF45A, FD233, FD238, and NL-4 (Anywhere New Material Co., Ltd.); phosphor powders including SCASN:Eu, β-SiAlON:Eu, LuAG:Ce, K₂SiF₆:Mn, and YAG:Ce (Grirem Advanced Materials Co., Ltd), CASN:Eu and BaSi₂O₂N₂:Eu (Shandong Yingguang Advanced Materials Co., Ltd), LSN:Ce (Mitsubishi Chemical Holdings), SrAl₂O₄:Eu,Dy (Shenzhen looking long technology Co., Ltd.), Ca-α-SiAlON:Eu (Denka Co., Ltd.), Gd₂O₂S:Tb (Shanghai Keyan Phosphor Technology Co.,Ltd); and YAG:Ce-PiG plate (Doctor Optotech Co., Ltd.) are all commercially available. To fabricate PiGF, we purchased terpeneol and ethyl cellulose from Aladdin China; sapphire wafers (10 × 10 × 0.3 mm and φ45 mm) from Xinxiang City Baihe O.E. Co., Ltd.; SiC single crystal wafers (10 × 10 × 0.5 mm) from Beijing Tanke Blue Semiconductor Co., Ltd; K9 glass wafers (10 × 10 × 0.3 mm) from Schott Glaswerke AG; and AlN ceramic wafers (10 × 10 × 0.3 mm) from Guangzhou Baile New Materials Technology Co., Ltd., respectively.

Fabrication of PiGF, PiGF phosphor wheel

The PiGF samples were prepared by co-sintering phosphors and glass powders on a high thermal conductivity substrate. The process started with the preparation of an organic solvent by dissolving 3 wt% ethyl cellulose in 97 wt% terpeneol by stirring at 80 °C for 8 h. Subsequently, phosphors and glass powders were measured in a specific mass ratio. These components were then thoroughly mixed with the organic solvent in an agate mortar to achieve a powder-to-gel mass ratio of 2:1. The resulting slurry was then applied to the high thermal conductivity substrate using an automatic coating machine, with the thickness of film meticulously controlled by the height of blade, which was accurate to within 10 µm. The samples were then subjected to a heat treatment in a muffle furnace at 300 °C for 3.5 h to ensure the complete volatilization of the organics, yielding a precursor PiGF. To complete the process, the precursor film was sintered either in an RTA device (RTP-500, estarlabs.com) or in a muffle furnace. The RTA process involved rapid heating to the set temperature – 450 °C, 500 °C, 550 °C, 600 °C, 650 °C, and 700 °C within 10 s, followed by soaking times ranging from 1 s to 30 s. In contrast, the muffle furnace sintering process was performed at a slower pace, with a heating rate of 5 °C min⁻¹ to the set temperature – 500 °C, 550 °C, 600 °C, 650 °C, and 700 °C – followed by soaking times ranging from 5 to 20 min. A similar method was used for the preparation of monochrome phosphor wheels, but with different sample quantities. The preparation steps for the patterned phosphor wheel are similar, except that a screen-printing machine (Kaivo Optoelectronic Technology Co., Ltd.) with a sector-shaped stencil is used for coating in the third step.

Characterizations

Phase determination of the prepared samples was conducted using a MiniFlex 600 powder X-ray diffractometer (Rigaku) with Cu K α radiation ($\lambda = 1.540593 \text{ \AA}$) over a data collection range of 10° – 70° at a scanning speed of 5° min^{-1} . Microstructural analysis was performed using SEM (JSM-6700F, JEOL, Japan and SU8010, HITACHI, Japan). TEM and HADDF-STEM images were acquired at room temperature using a spherical aberration-corrected STEM (JEM-ARM 200 F; JEOL, Japan). The electron-transparent cross-sectional STEM specimen was prepared by focused ion beam milling (Helios G4; FEI/Thermo Fisher Scientific, USA) and further thinned by focused Ar-ion milling (Nano-Mill 1040; Fischione Instruments, Export, PA, USA). The elemental distribution within the PiGFs was analyzed using XRF spectrometer (M4 Tornado, Bruker, Germany). The distribution of phosphor particles on the surface of PiGF was examined using an optical microscope (HD, LUO SI, China). The 3D distribution of phosphor particles within the PiGF was investigated using CLSM with an excitation wavelength of 405 nm (A1 MP, Nikon, Japan). The surface roughness of the PiGF was analyzed using a white light interferometer (LAMBDA, RTEC, USA). Sample porosity distribution and porosity analysis were carried out by using micro-CT (Nanovoxel-3432E, Sanying Precision Instruments, China). To be mentioned, the pores smaller than 500 nm cannot be detected due to the resolution limit of CT scanner. The thermodynamic parameters were determined using a DTA instrument (STA449 F5, Netzsch, Germany). The refractive index of glass sample was measured by a digital refractometer (RDB, GEM Instruments). The full transmission spectra were recorded by using a UV-visible-NIR spectrophotometer (Lambda 950, Perkin Elmer). The IQE of luminescence was measured based on a 455 nm semiconductor laser (3 W), an integrating sphere, a cooling-heating stage, and a fiber optic spectrometer. The integrating sphere was assembled onto a cooling-heating stage, and the luminescence signal was transmitted to the spectrometer (Ocean Optics, QE pro) via a fiber. IQE was calculated by the ratio of emitted to absorbed photons. The PL and PLE spectra, as well as fluorescence decay curves, were recorded using a fluorescence spectrometer (FLS920, Edinburgh Instruments) equipped with a 400 W xenon lamp and a 470 nm pulsed laser source. Samples were placed on a cooling-heating stage (Linkam Scientific Instruments, THMS600E) and held for 2 min at different temperatures before temperature-dependent PL spectrum measurements were taken. The photometric parameters of the samples under blue laser excitation were collected using a homemade laser illumination system, which consisted of a custom-made integrating sphere with a diameter of 10 cm, a 22 W blue laser (Ningbo Yuanming Photoelectric, LSR455CP), and a fiber optic spectrometer (Ocean Optics, QEpro). It should be noted that the incident 22 W blue laser inevitably experiences losses after passing through the lens, resulting in a maximum light power of 17 W actually reaching the sample. The testing optical path was set in a reflective mode, with the incident laser spot having an approximately circular shape and an area of about 0.628 mm^2 . The sample was adhered to a rotating aluminum wheel that was driven by a high-speed rotating motor with a rotation speed of 3000 rpm. The optical power of the blue laser was measured using a laser power meter equipped with a thermopile power probe (model 30A-BB-18, Ophir).

Finite element analyses

The rapid thermal annealing (RTA) system modelling. To explore the feasibility of bulk sample preparation through the RTA process, finite element modeling was conducted using Ansys software to investigate the temperature distribution across various regions of the silicon wafer during the process. The three-dimensional model and computational domain are depicted in Fig. 1c. The upper and lower arrays of halogen tungsten lamps within the quartz chamber of the furnace were simplified as two planar radiation sources with a diameter of 170 mm, with their temperatures set at 3225 K; the dimensions of the

quartz chamber are 170 mm in length, 200 mm in width, and 20 mm in height, with a wall thickness of 2 mm; a silicon wafer with a diameter of 101.6 mm (4 inches) and a thickness of 1 mm is positioned at the center of the quartz chamber. The wafer is uniformly covered with a 5×5 array of 25 glass film-sapphire precursor composite materials. The quartz chamber is sealed to allow infrared radiation emitted by the radiation source to pass through, thereby heating the silicon wafer and the samples. In this case, the silicon wafer is placed in an atmospheric environment.

It should be noted that in our scenario, the metal casing and water or air cooling systems outside the computational domain were not considered, which may deviate from the actual conditions. However, we believe that during the heating and temperature stabilization phases, the impact of these factors is minimal and does not affect our discussion on the uniformity of temperature distribution across the silicon wafer and samples during the heating process. These elements can be disregarded in the simulation.

Theoretical basics

The radiation transfer process was investigated using the Discrete Ordinates (DO) radiation model. Additionally, the simulation process was coupled with the energy equation, taking into account the heat conduction within the solid materials and the heat convection process at the material-air boundary.

The radiative heat transfer process is governed by the Radiative transport equation (RTE):

$$\nabla \cdot (I(r, \mathbf{s})\mathbf{s}) + (a + \sigma_s)I(r, \mathbf{s}) = an^2 \frac{\sigma T^4}{\pi} + \frac{\sigma}{4\pi} \int_0^{4\pi} I(r, \mathbf{s}')\Phi(\mathbf{s}, \mathbf{s}')d\Omega' \quad (1)$$

the term $\nabla \cdot (I(r, \mathbf{s})\mathbf{s})$ represents the rate of change of the radiative intensity with respect to the spatial coordinate r and direction \mathbf{s} , essentially describing the propagation rate of light rays. This term accounts for the variation in radiative intensity. The term $(a + \sigma_s)I(r, \mathbf{s})$ ($a + \sigma_s$)(r, \mathbf{s}) denotes the absorption term, where a is the absorption coefficient and σ_s is the scattering coefficient. $I(r, \mathbf{s})$ represents the radiative intensity at a given position r and direction \mathbf{s} . This term describes the reduction in radiative intensity due to absorption and scattering processes. The term $\frac{an^2\sigma T^4}{\pi}$ is the emission term, where n is the refractive index, σ is the Stefan-Boltzmann constant, and T is the temperature. It signifies the increase in radiative intensity due to the emission from the object. Lastly, the term $\frac{\sigma}{4\pi} \int_0^{4\pi} I(r, \mathbf{s}')\Phi(\mathbf{s}, \mathbf{s}')d\Omega'$ represents the scattering term, which accounts for the changes in radiation due to scattering. $\Phi(\mathbf{s}, \mathbf{s}')$ is the phase function, characterizing the probability of radiation being scattered from direction \mathbf{s}' to direction \mathbf{s} . The integral is taken over 4π , indicating the integration over all possible incident directions \mathbf{s}' .

In the simulation process, the DO radiation model is coupled with the energy equation. The energy equation typically takes into account the conservation of energy and can be expressed as follows:

$$\frac{\partial(\rho E)}{\partial t} + \nabla \cdot [\mathbf{V}(\rho E + p)] = \nabla \cdot [k_{\text{eff}} \nabla T - \sum h_i \mathbf{j}_i + \tau_{\text{eff}} \cdot \mathbf{V}] + S_h \quad (2)$$

The term $\frac{\partial(\rho E)}{\partial t}$ is the unsteady term, which signifies the rate of change of the total energy per unit volume, ρE , with respect to time t . Here, ρ denotes the fluid density, and E represents the total energy per unit mass, encompassing internal energy, kinetic energy, and energy attributable to pressure. The term $\nabla \cdot [\mathbf{V}(\rho E + p)]$ is referred to as the convective term, which describes the energy transported by the motion of the fluid. Here, \mathbf{V} is the velocity vector, and p is the pressure. This term employs the divergence $\nabla \cdot$ to depict how energy is conveyed through space via the fluid's motion. The term $\nabla \cdot [k_{\text{eff}} \nabla T]$ represents the heat conduction term, which describes the energy transfer due to thermal conduction. Here, k_{eff} is the effective thermal conductivity,

T denotes the temperature, and ∇T signifies the temperature gradient. The term $\sum h_j j$ is known as the diffusive term, which accounts for the energy changes due to the diffusion of multiple species. In this context, h_j represents the specific enthalpy of the j -th species, and j denotes the diffusion flux of that species. The term $\tau_{\text{eff}} \cdot \mathbf{V}$ represents the viscous dissipation term, which signifies the mechanical energy dissipation due to the viscous effects of the fluid. Here, τ_{eff} is the effective stress tensor, which characterizes the viscous forces within the fluid, and \mathbf{V} is the fluid velocity vector. The term S_h is referred to as the enthalpy source term, which signifies the presence of external or internal energy sources.

Equation (1) describes the process of radiative transfer, while Eq. (2) considers the conservation of energy. The connection between the two lies in the fact that radiation is a form of energy transfer, and in complex systems, radiation interacts with other mechanisms of energy transfer, such as heat conduction and convection, affecting the temperature field and energy balance. Consequently, in systems where radiative heat transfer is involved, these two equations must be solved in conjunction.

Numerical simulation

Utilizing the Ansys software suite, a numerical simulation of the rapid thermal annealing (RTA) system was conducted. The model encompassed a substantial number of elements, totalling 1,644,875, and nodes, amounting to 1,868,928. The temporal discretization was set at intervals of 0.5 s, with radiative iterations performed every 0.5 s, each comprising ten energy iterations (Supplementary Movie 2). This interval was deemed sufficiently small to resolve the rapid thermal transport processes. The simulated heating segment was calibrated to align with the optimal process time identified in the experimental phase, specifically targeting a temperature of 550 °C for a duration of 10 s.

Reporting summary

Further information on research design is available in the Nature Portfolio Reporting Summary linked to this article.

Data availability

The data that support the findings of this study are available from the corresponding author upon request. Source data are provided with this paper.

References

- Wierer, J. J., Tsao, J. Y. & Sizov, D. S. Comparison between blue lasers and light-emitting diodes for future solid-state lighting. *Laser Photonics Rev.* **7**, 963–993 (2013).
- Wang, L., Xie, R. J., Suehiro, T., Takeda, T. & Hirosaki, N. Down-conversion nitride materials for solid state lighting: recent advances and perspectives. *Chem. Rev.* **118**, 1951–2009 (2018).
- Li, S. X., Wang, L., Hirosaki, N. & Xie, R. J. Color conversion materials for high-brightness laser-driven solid-state lighting. *Laser Photonics Rev.* **12**, 1800173 (2018).
- Zhang, R. et al. A new-generation color converter for high-power white LED: transparent Ce^{3+} :YAG phosphor-in-glass. *Laser Photonics Rev.* **8**, 158–164 (2014).
- Chen, D. Q., Xiang, W. D., Liang, X. J., Zhong, J. S. & Ding, M. Y. Advances in transparent glass-ceramic phosphors for white light-emitting diodes—a review. *J. Eur. Ceram. Soc.* **35**, 859–869 (2015).
- Balci, M. H. et al. Comparative study of blue laser diode driven cerium-doped single crystal phosphors in application of high-power lighting and display technologies. *Opt. Rev.* **25**, 166–174 (2018).
- Chen, W. et al. Enhancing luminous flux and color rendering of laser-excited YAG:Ce³⁺ single crystal phosphor plate via surface roughening and low-temperature. *J. Lumin.* **251**, 119225 (2022).
- Fu, J. et al. Elaboration of Ce:(Lu,Gd)₃Al₅O₁₂-Al₂O₃ transparent nanoceramics through full glass crystallization for high-power white LED/LD lighting. *J. Mater. Chem. C.* **11**, 16186–16194 (2023).
- Wu H. J. et al. Cyan-green-emitting Ca₃Sc₂Si₃O₁₂:Ce³⁺ transparent ceramics: a promising color converter for high-brightness laser lighting. *J. Adv. Ceram.* **12**, 1731–1741 (2023).
- Yang, Z. Y. et al. Thermally stable red-emitting oxide ceramics for laser lighting. *Adv. Mater.* **35**, 2301837 (2023).
- Chen, H. et al. High luminous efficiency and high saturation threshold in highly transparent LuAG:Ce phosphor ceramics for laser diodes lighting. *Opt. Express* **32**, 2644–2657 (2024).
- Huang, P. et al. Nano wave plates structuring and index matching in transparent hydroxyapatite-YAG: Ce composite ceramics for high luminous efficiency white light-emitting diodes. *Adv. Mater.* **32**, 1905951 (2020).
- Gao, J. et al. Cold sintering of highly transparent calcium fluoride nanoceramic as a universal platform for high-power lighting. *Adv. Funct. Mater.* **33**, 2302088 (2023).
- Zhu, Q. Q. et al. A robust red-emitting phosphor-in-glass (PiG) for use in white lighting sources pumped by blue laser diodes. *J. Alloy Compd.* **702**, 193–198 (2017).
- Lee, Y. K., Kim, Y. H., Heo, J., Im, W. B. & Chung, W. J. Control of chromaticity by phosphor in glasses with low temperature sintered silicate glasses for LED applications. *Opt. Lett.* **39**, 4084–4087 (2014).
- Lin, H., Hu, T., Cheng, Y., Chen, M. X. & Wang, Y. S. Glass ceramic phosphors: towards long-lifetime high-power white light-emitting-diode applications—a review. *Laser Photonics Rev.* **12**, 1700344 (2018).
- Zhang, D. et al. Highly efficient phosphor-glass composites by pressureless sintering. *Nat. Commun.* **11**, 2805 (2020).
- You, S. H. et al. A thermally robust La₃Si₆N₁₁:Ce-in-glass film for high-brightness blue-laser-driven solid state lighting. *Laser Photonics Rev.* **13**, 1800216 (2018).
- Jiang, Z. et al. High color rendering and high-luminance laser lighting using all inorganic nitride phosphor films. *RSC Adv.* **13**, 25561–25570 (2023).
- Wang, G. J. et al. Innovative architecture for phosphor-in-glass films enabling superior luminance and color quality laser-driven white light. *Laser Photonics Rev.* **18**, 2301263 (2024).
- Yoshimura, K. et al. Optical properties of solid-state laser lighting devices using SiAlON phosphor-glass composite films as wave-length converters. *Jpn J. Appl Phys.* **55**, 042102 (2016).
- Lin, S. S. et al. Highly crystalline Y₃Al₅O₁₂:Ce³⁺ phosphor-in-glass film: a new composite color converter for next-generation high-brightness laser-driven lightings. *Laser Photonics Rev.* **16**, 2200523 (2022).
- Zhang, J. D. et al. High-efficiency phosphor-in-glass with ultra-high color rendering indexing for white laser diode lighting. *Ceram. Int* **48**, 1682–1689 (2022).
- Liao, S. X. et al. Novel color converters for high brightness laser-driven projection display: transparent ceramics-glass ceramics film composite. *Adv. Funct. Mater.* **34**, 2307761 (2023).
- Deng, T. L., Chen, H. X., Hei, L. L., Li, S. X. & Xie, R. J. Achieving high light uniformity laser-driven white lighting source by introducing secondary phases in phosphor converters. *J. Inorg. Mater.* **37**, 891–898 (2022).
- Wang, P. F., Sui, P., Lin, S. S., Lin, H. & Wang, Y. S. Lu₂SrAl₄SiO₁₂:Ce³⁺ phosphor in glass film-on-sapphire and its application to laser lighting. *Chin. J. Lumin.* **42**, 1493–1501 (2021).
- Zhang, Y. J. et al. A high quantum efficiency CaAlSiN₃:Eu²⁺ phosphor-in-glass with excellent optical performance for white light-emitting diodes and blue laser diodes. *Chem. Eng. J.* **401**, 125983 (2020).

28. Zhang, J. F., Tu, R. & Goto, T. Fabrication of transparent SiO₂ glass by pressureless sintering and spark plasma sintering. *Ceram. Int.* **38**, 2673–2678 (2012).
29. Wang, C. W. et al. A general method to synthesize and sinter bulk ceramics in seconds. *Science* **368**, 521–526 (2020).
30. Liang, Y. F. et al. Phosphor-in-glass (PIG) converter sintered by a fast Joule heating process for high-power laser-driven white lighting. *Opt. Express* **29**, 14218–14230 (2021).
31. Peng, Y. et al. Rapid and efficient preparation of phosphor-in-glass converter by induction heating for high-power white LEDs/LDs. *Mater. Today Commun.* **29**, 102839 (2021).
32. Lin, Z. W. et al. Rapid pressureless sintering of glasses. *Small* **18**, 2107951 (2022).
33. Yoo, J. H. et al. Ultra-fast fabrication of phosphor in glass via laser sintering using silicon wafers. *J. Alloy Compd.* **976**, 173139 (2024).
34. Sun, Y. S. et al. Rapid synthesis of phosphor-glass composites in seconds based on particle self-stabilization. *Nat. Commun.* **15**, 1033 (2024).
35. Huang, Q. G. et al. Patterned glass ceramic design for high-brightness high-color-quality laser-driven lightings. *J. Adv. Ceram.* **11**, 862–873 (2022).
36. Huang, Q. G. et al. Toward high-quality laser-driven lightings: chromaticity-tunable phosphor-in-glass film with “phosphor pattern” design. *Laser Photonics Rev.* **16**, 2200040 (2022).
37. Lin, Y. et al. CaLu₂Mg₂Si₃O₁₂:Ce³⁺, Cr³⁺, Nd³⁺ phosphor-in-glass film for laser-driven ultra-broadband near-infrared lighting with watt-level output. *Laser Photonics Rev.* **18**, 2400995 (2024).
38. Chung W. J. & Nam Y. H. Review—a review on phosphor in glass as a high power LED color converter. *ECS J. Solid State Sci. Technol.* **9**, 016010 (2019).
39. Wei, Y. L., Ebendorff-Heidepriem, H. & Zhao, J. B. Recent advances in hybrid optical materials: integrating nanoparticles within a glass matrix. *Adv. Opt. Mater.* **7**, 1900702 (2019).

Acknowledgements

This work was supported by National Natural Science Foundation of China (No.52372161 to L.H., No.U2005213 to W.Y.S. and No.12274408 to W.Y.S.), Science Fund for Distinguished Young Scholars of Fujian Province (No.2022J06030 to L.H.), Science Fund of Fujian Province (No.2023J01217 to C.Y.), Fujian Science & Technology Innovation Laboratory for Optoelectronic Information of China (No.2021ZR134 to L.H.), and Self-deployment Project Research Program of Haixi Institutes, Chinese Academy of Sciences (No.CXZX-2022-GH11 to L.H.).

Author contributions

L.H. conceived the initial concept. W.P.F. synthesized the materials and drafted the initial manuscript. L.H. assisted W.P.F. in analyzing the

experimental results and in completing the final draft. C.G.X. contributed to the characterization of the microstructure. W.W.T. documented the sintering curves. X.Y. provided assistance in the demonstration of applications. C.Y. offered constructive suggestions on data analysis. L.Y. and X.J. aided in conducting spectral measurements. W.Y.S. oversaw the project.

Competing interests

The authors declare no competing interests.

Additional information

Supplementary information The online version contains supplementary material available at <https://doi.org/10.1038/s41467-025-58099-5>.

Correspondence and requests for materials should be addressed to Hang Lin or Yuansheng Wang.

Peer review information *Nature Communications* thanks Tomokatsu Hayakawa, Zhiguo Xia, Dae-Ho Yoon and the other, anonymous, reviewer(s) for their contribution to the peer review of this work. A peer review file is available.

Reprints and permissions information is available at <http://www.nature.com/reprints>

Publisher's note Springer Nature remains neutral with regard to jurisdictional claims in published maps and institutional affiliations.

Open Access This article is licensed under a Creative Commons Attribution-NonCommercial-NoDerivatives 4.0 International License, which permits any non-commercial use, sharing, distribution and reproduction in any medium or format, as long as you give appropriate credit to the original author(s) and the source, provide a link to the Creative Commons licence, and indicate if you modified the licensed material. You do not have permission under this licence to share adapted material derived from this article or parts of it. The images or other third party material in this article are included in the article's Creative Commons licence, unless indicated otherwise in a credit line to the material. If material is not included in the article's Creative Commons licence and your intended use is not permitted by statutory regulation or exceeds the permitted use, you will need to obtain permission directly from the copyright holder. To view a copy of this licence, visit <http://creativecommons.org/licenses/by-nc-nd/4.0/>.

© The Author(s) 2025